JGR Atmospheres

RESEARCH ARTICLE
10.1029/2025JD044311

Estimating the Impact of Impounding an 85-km^2 Hydropower Reservoir in a Subarctic Environment on the Local Radiation Balance

Imen Ben Aba[1], Daniel F. Nadeau[1], Jean-Daniel Sylvain[2,3], Guillaume Drolet[2], and François Anctil[1]

[1]Department of Civil and Water Engineering, Université Laval, Québec, QC, Canada, [2]Direction de la recherche forestière, Ministère des Ressources naturelles et des Forêts, Québec, QC, Canada, [3]Hydrology, Climate and Climate Change Laboratory, École de technologie supérieure, Université du Québec, Montréal, QC, Canada

Key Points:

- The impoundment of a subarctic reservoir notably raised winter albedo while lowering summer albedo
- Reservoir impoundment altered seasonal temperatures, delaying peaks by 3–5 weeks and warming autumn/winter while cooling spring/summer
- Reservoir impoundment induced −21 W m^{-2} net cooling, with winter deficit (−60 to −140 W m^{-2}) exceeding summer surplus (+5 to +50 W m^{-2})

Correspondence to:

I. Ben Aba,
imen.ben-aba.1@ulaval.ca

Citation:

Ben Aba, I., Nadeau, D. F., Sylvain, J.-D., Drolet, G., & Anctil, F. (2025). Estimating the impact of impounding an 85-km^2 hydropower reservoir in a subarctic environment on the local radiation balance. *Journal of Geophysical Research: Atmospheres*, *130*, e2025JD044311. https://doi.org/10.1029/2025JD044311

Received 4 JUN 2025
Accepted 9 OCT 2025

Abstract This study focuses on the net radiative forcing caused by the impoundment of an 85-km^2 hydroelectric reservoir in the subarctic Côte-Nord, Quebec, Canada (50.69°N, 63.24°W, mean depth of 44 m). Using spectral bands from the Landsat 7 ETM+ and Landsat 8 OLI/TIRS satellites, we observed spatial and temporal variations in albedo and surface temperature on 104 dates between 2000 and 2023. By integrating these data with ERA5-Land meteorological reanalyses and in situ measurements, we investigated seasonal and interannual variations in shortwave and longwave radiative fluxes and net radiation before (2000–2013) and after (2015–2023) reservoir impoundment. The flooded area initially consisted of 79% coniferous forest (mainly black spruce), 15% water, 4% dry soil, and 2% wet soil. Before the impoundment, the average winter albedo was 0.25 ± 0.02 and the summer albedo was 0.08 ± 0.002. After the impoundment, the winter albedo increased significantly, reaching between 0.70 and 0.90 in the presence of fresh snow on the ice (January to May), while in summer it decreased to about 0.05 ± 0.003. Surface temperatures exhibited pronounced pre- to postimpoundment contrasts, with the reservoir consistently 2–7°C warmer in autumn and winter but 1–5°C cooler in spring and summer. The reservoir also reaches its maximum temperature 3–5 weeks later. The impoundment induced a net radiative cooling of −21 W m^{-2} compared to forest, featuring a pronounced winter deficit (−60 to −140 W m^{-2}) due to snow cover albedo effects, partially compensated by summer surpluses (+5 to +50 W m^{-2}).

Plain Language Summary Hydropower is a strategic solution for reducing CO_2 emissions in the face of population growth and increasing energy demand. However, it is essential to assess the regional climate impacts of hydropower reservoirs in order to plan these projects effectively and ensure a successful energy transition. Land use changes associated with impoundment affect albedo and surface temperature, thereby influencing the local radiation balance. This article analyzes the impact of the implantation of a hydroelectric reservoir (50.69°N, 63.24°W) on the local climate in a subarctic environment. The study shows that the installation of the reservoir led to a cooling of the local climate by −21 W/m^2. This cooling is mainly due to an increase in the annual albedo of the reservoir compared to the previous land use, which was mainly forested. This effect is particularly pronounced at higher latitudes, where snow and ice are present for much of the year, increasing the reflection of sunlight. In addition, slight surface warming in winter and autumn and cooling in spring and summer have been observed following the impoundment. This study highlights the importance of thorough assessment of local climate impacts from hydropower projects to validate their environmental benefits.

1. Introduction

According to the International Hydropower Association (IHA), global hydropower capacity had reached 1,416 GW in 2023, with a total production of 4,185 TWh, highlighting the central role of hydropower in the energy transition. To meet the COP28 targets, it is imperative to accelerate investment and ensure annual growth of 25 GW. In addition, a doubling of capacity will be needed after 2030 to achieve carbon neutrality by 2050 (IHA, 2024). Hydropower plants emit significantly less carbon dioxide than fossil fuel power plants (Levasseur et al., 2021), preventing the release of approximately three gigatons of CO_2 per year or about 9% of global emissions (IEA, 2022).

However, the construction of hydroelectric reservoirs inevitably leads to changes in land use that can affect the local radiation balance. This begins with the flooding of existing terrestrial ecosystems such as forests, grasslands, and wetlands, or the widening of existing watercourses. These changes alter surface albedo, the ratio of reflected to incident solar radiation. Albedo is an essential parameter of the net radiation R_n, influencing energy exchange at the Earth's surface-atmosphere interface. R_n results from the balance between net shortwave radiation (R_{Sn}) and net longwave radiation (R_{Ln}) and can be expressed as follows:

$$R_n = R_{Sn} + R_{Ln} = R_{S\downarrow} - R_{S\uparrow} + R_{L\downarrow} - R_{L\uparrow} \quad (1)$$

where $R_{S\downarrow}$ is the incoming shortwave (solar) radiation, $R_{S\uparrow}$ is the reflected shortwave radiation, $R_{L\downarrow}$ is the incoming longwave (atmospheric) radiation, and $R_{L\uparrow}$ is the longwave radiation emitted and reflected by the Earth. In particular, the reflected shortwave radiation is dependent on the incident shortwave radiation and the surface properties:

$$R_{S\uparrow} = \alpha R_{S\downarrow} \quad (2)$$

where α is the surface albedo, while the emitted and reflected longwave radiation is dependent on the surface temperature (T_s), the incident longwave radiation and the surface properties:

$$R_{L\uparrow} = \varepsilon\sigma T_s^4 + (1-\varepsilon) R_{L\downarrow} \quad (3)$$

where ε is the surface emissivity and σ is the Stefan-Boltzmann constant (5.67×10^{-8} W m^{-2} K^{-4}).

Hydroelectric reservoirs change the surface albedo, which alters the local radiation balance and in turn affects local climatic conditions. This impact is closely linked to factors such as reservoir size and geography. For example, Wohlfahrt et al. (2021) examined the impact of albedo change due to impoundment of hydroelectric reservoirs on a global scale, highlighting that positive radiative forcing was observed for 5% of the reservoirs considered (latitude >44°N). This effect reduces the climate benefits from the negative radiative forcing associated with hydropower generation. However, snow cover and ice cover increase albedo compared to the surrounding landscape in 5% of reservoirs considered in their analysis, reducing radiative forcing. Some studies have provided valuable insights into the impact of northern reservoirs on changes in temperature regimes. For example, a modeling study by Irambona et al. (2018) compared regional climate simulations with and without the presence of hydroelectric reservoirs in Northern Quebec (Canada). The results show that these reservoirs induce a winter warming of $+0.7 \pm 0.02$°C and a summer cooling of -0.3 ± 0.02°C, mainly due to the reduction in albedo and the high heat capacity of the water bodies. Similarly, Martynov et al. (2012) simulated an average warming of 6°C in January and an average cooling of 2°C in June over Lake Superior using the Canadian Regional Climate Model (CRCM5) in which two one-dimensional lake models, FLake (FL) and Hostetler (HL), were interactively coupled. The authors compared reanalysis-forced multidecadal climate simulations over a 50-year period (1959–2008) with and without interactive lakes to assess their impact on the regional climate of North America. Onwukwe et al. (2024) analyzed the climatic impacts of the Williston Reservoir in British Columbia using high-resolution simulations of the Weather Research and Forecasting (WRF) meteorological model over a 10-year period. Comparing simulations with and without the reservoir, they found an 11.5% increase in autumn precipitation (up to 30 mm), a significant decrease in summer precipitation due to reduced convection, and a 0.2–0.5°C increase in the mean annual temperature within 10 km of the reservoir, mainly in autumn. Li et al. (2023) investigated the climate impact of dams on the Jinsha River in southwest China, using 40 years of reanalysis data at 90 m resolution combined with a long- and short-term memory model (LSTM) to develop an index of the effect of water impoundments on temperature. Comparing the periods before (1980–2012) and after (2013–2019) the construction of the dams, they observed a decrease of 0.4°C in the annual maximum temperature, while the mean and minimum temperatures increased by 0.1°C and 1.0°C, respectively. The warming effects were more pronounced during the dry season and at higher altitudes, while cooling effects were observed within a 4-km radius of the reservoirs.

Canada, the world's third largest producer of hydroelectricity, generated 393,789 gigawatt-hours in 2022, or 61.7% of its total electricity production (Natural Resources Canada, 2024). In 2021, the country had 595 hydroelectric plants (Natural Resources Canada, 2024). As the largest producer of hydroelectricity in Canada,

Quebec generates about 95% of its energy needs from this source (Canada Energy Regulator, 2024). In 2022, the province produced more than 200 TWh of hydroelectricity, accounting for 40% of national production (Natural Resources Canada, 2024). The province has some of the largest hydroelectric reservoirs in the world, including those in the James Bay (La Grande) and Manicouagan-Outardes complexes. As of 2024, Hydro-Québec operates 63 hydroelectric power plants with a total installed capacity of 38,400 MW (Hydro-Québec, 2024).An emblematic project, the Romaine project, includes four power stations on the Romaine River and was completed with the commissioning of Romaine-4 in September 2022. This 1,550 MW project was a major investment in the province's infrastructure, helping to increase renewable electricity production and strengthen Quebec's position in the energy transition (Hydro-Québec, 2007). Although Quebec is a major player in the sector, research on the environmental and social impacts of hydropower projects remains relatively limited.

In a recent study, Pierre et al. (2023) analyzed the thermal regime and energy balance of the Romaine-2 reservoir, observing thermal stratification from June to November in summer and from December to May in winter. Net radiation accounts for 95.6% of the energy input, while heat advection contributes little (4.4%). Given that latent (58.5%) and sensible (16.5%) heat fluxes correspond to 75% of the output on energy balance, it is important to characterize their temporal dynamic of the reservoir's annual energy budget.

Although hydropower represents a major source of renewable energy in Québec, the impacts of reservoirs on the local radiative balance and seasonal surface energy dynamics remain poorly understood, particularly under conditions of intermittent snow and ice cover. These local radiative effects could contribute to the net climate balance, alongside the benefits gained from reducing fossil fuel emissions. This knowledge gap limits our understanding of the role of such infrastructures in modulating surface atmosphere interactions and influencing regional climate. In this context, this study aims to analyze the impact of the 85-km^2 Romaine-2 reservoir impoundment on the seasonal dynamics of the local radiation balance, focusing on changes characterized by the intermittent presence of ice and snow. To achieve this goal, satellite images with a spatial resolution of 30 m were acquired both before (2000–2013) and after (2015–2023) the reservoir's impoundment to monitor changes in surface albedos and surface temperatures. These data are then used in combination with ERA5-Land reanalysis data and local hydrometeorological observations to estimate the total net radiation before and after the construction of the reservoir.

2. Materials and Methods

2.1. Study Site and Local Measurements

The study site is part of the Romaine River hydroelectric complex in the Côte-Nord region of Quebec, Canada. The complex is operated by Hydro-Québec, a state-owned organization responsible for the production and distribution of electricity in Quebec. The complex consists of four hydropower plants with a total installed capacity of 1,550 MW. This study focusses on the Romaine-2 reservoir, which has a capacity of 640 MW. The Romaine-2 reservoir (50.69°N, 63.24°W; Figure 1a) was flooded in 2014 and is now a dimictic water body that is ice-free from May to December. The reservoir has an average depth of 44 m, a maximum depth of 101 m, and a surface area of 85.6 km^2 when full. It has an elongated shape oriented on a north-south axis. Figure 1b shows the contour of the reservoir at its maximum water level. This contour was used in this study to extract pixels for averaging albedo values.

The regional climate is characterized by an annual precipitation of 1,167 mm and an mean annual air temperature of 1°C over the period 2018–2022. During this period, extreme temperatures ranged from −28°C to +22°C (Kallel et al., 2024; Pierre et al., 2023). Average evaporation from reservoirs was estimated at 590 ± 66 mm, accounting for about 51% of the annual precipitation with episodic peaks in evaporation occurring between August and December (Kallel et al., 2024; Pierre et al., 2023).

Before the reservoir was impounded, 79% of the area was dominated by forest, 15% by water bodies, 4% by dry bare soil, and 2% by wetlands. The forest is dominated by coniferous stands, composed of tree species typical of the boreal forest. Coniferous stands (93%) are primarily characterized by black spruce (Picea mariana (Mill.) B.S.P.) and balsam fir (Abies balsamea (L.) Mill). Mixed stands (6%) consist of black spruce and white birch (Betula papyrifera, Marsh.), while deciduous stands feature white birch and aspen (Populus tremuloides Michx). Table 1 summarizes the land cover before the reservoir was impounded.

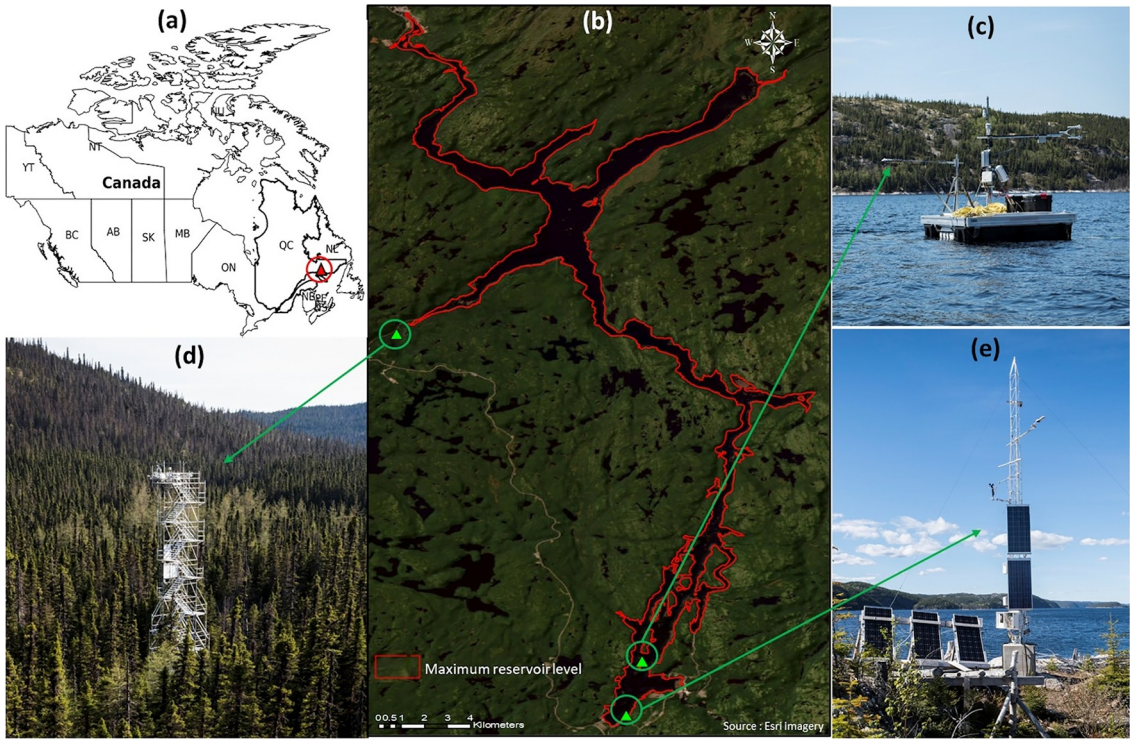

Figure 1. (a) Location of the Romaine-2 reservoir in North America; (b) area covered by Romaine-2 hydroelectric reservoir; (c) reservoir flux tower, deployed only from June to October; (d) forest flux tower; (e) shore flux tower. Photos were provided by Hydro-Québec.

Since 2018, three flux towers have been operating in the study area: one above the forest canopy (Figure 1d), one on the Romaine-2 reservoir (Figure 1c, available only in ice-free conditions, from June to October, to avoid damage associated with the action of ice), and one along its shore (Figure 1e). Four-component net radiometers (CNR4, Kipp & Zonen, OTT HydroMet B.V., The Netherlands) were installed on the towers to measure net radiation, capturing incoming and outgoing solar and infrared radiation.

Snow depth measurements were conducted between 2021 and 2023 at the study site in two contrasting forest environments: (a) an undercanopy site, defined as being directly under the forest canopy, and (b) a gap site, corresponding to an opening in the canopy of approximately 4–5 m in diameter, without shrub vegetation.

To quantify snow depth, automatic sensors were installed at a height of 2.5 m above ground level at each site. Ultrasonic snow height sensors were deployed to monitor snow depth. Judd Communication sensors (Judd Communication, USA) were used under cover during the winter of 2021–2022, while SR50 sensors (Campbell Scientific, USA) were used at both sites during the winter of 2022–2023. These instruments continuously measure the distance between the sensor and the snow surface, providing snow height data with centimeter accuracy. The time series derived from these measurements allow for the analysis of the snow accumulation and melt dynamics in relation to the structural characteristics of the forest cover.

Table 1
Summary of Land Cover Before Reservoir Installation

Land cover type	Area covered (%)
Forest stands:	79
- 93% conifers, - 6% mixed species, - 1% deciduous	
Water bodies	15
Dry bare soil	4
Wetlands	2

2.2. Surface Albedo and Temperature Retrieval From Satellite Data

2.2.1. Satellite Data Acquisition

All of the satellite data used in this study were queried and processed using the Google Earth Engine (GEE) platform to reduce data management overhead and to speed up the analysis process (Gorelick et al., 2017). This study is based on a time series of Landsat 8 TOA Tier 1 Collection 1 images (available from 2013) with a spatial resolution of 30 m and Landsat 7 TOA Tier 1 Collection 1 images available since 1999.

Landsat 7, launched on 15 April 1999, is equipped with the Enhanced Thematic Mapper Plus (ETM+) sensor, acquiring images with a swath of 185 km and a temporal resolution of 16 days. Its spectral bands (visible, near infrared—NIR, shortwave infrared - SWIR) offer a spatial resolution of 30 m, while the thermal band has a resolution of 60 m. From 2003 onward, a failure of the Scan Line Corrector (SLC-off) led to systematic gaps covering around 22% of the scenes, particularly in the periphery (Storey et al., 2005). Despite this limitation, Landsat 7 SLC-off data remain viable through spatial compensation techniques, such as kriging (Zhu et al., 2012) or specific masking of affected areas. Landsat 7 has thus played a critical role in maintaining the continuity of the Landsat archive, thus preserving essential time series for long-term Earth observation (Wulder et al., 2022). Detailed spectral specifications for Landsat 7 are provided in Appendix A (Table A1).

Landsat 8, operational since 11 February 2013, carries two improved sensors: the Operational Land Imager (OLI) and the Thermal Infrared Sensor (TIRS). Compared with ETM+, these sensors offer (a) additional spectral bands (including a cirrus band and an ultrablue band), (b) improved radiometric resolution (12 bits instead of 8 bits), and (c) better calibration (Hansen & Loveland, 2012; Irons et al., 2012). The satellite, in a Sun-synchronous orbit at an altitude of 705 km, covers a swath of 185 km with a cycle of 16 days. Notably, the OLI bands (visible to SWIR) offer a spatial resolution of 30 m, while the TIRS bands (thermal infrared) have a nominal resolution of 100 m (Montanaro et al., 2014). The detailed spectral characteristics of these sensors are presented in Table A1 in Appendix A. The time series used combines Landsat 7 (2000–2013) and Landsat 8 (2014–2023) images from Tier 1 TOA collections (L1TP correction level). Cloud masking was applied using the integrated quality assessment (QA) bands, and images with >30% cloud cover were excluded. Of the 451 scenes available, 104 were selected for analysis (Appendix A, Table A2).

2.2.2. Estimation of Surface Albedo

To produce the broadband surface albedo database from Landsat 7 and 8 images, a data processing pipeline was established. After image pretreatment for cloud masking, Landsat 7 and 8 images at the top of the atmosphere (TOA) were converted to surface reflectance using the 6S atmospheric correction model (Vermote et al., 1997), accessed through the Py6S implementation (Wilson, 2013). This process is based on an implementation in GEE by Nguyen et al. (2020), derived from a script developed by Murphy (2018). The 6S model was used to simulate radiative transfer in the Sun-Earth-surface-satellite-sensor system. Solving the radiative transfer equations required the specification of standardized atmospheric parameters. The midlatitude summer and midlatitude winter gas profiles were selected to represent summer and winter conditions, respectively. For aerosols, the standard continental model was applied. The required atmospheric data were obtained from several sources: ozone concentrations (O_3) were derived from measurements by the OMI instrument (NASA), aerosol optical thickness (AOT) was derived from MODIS products, and atmospheric water vapor content was derived from a combination of MODIS and MISR. In order to reduce biases associated with topographic variations, particularly those induced by slope, orientation, and elevation, a topographic correction was applied. This is based on the use of the NASA SRTM digital elevation model (DEM) with a spatial resolution of 30 m and the modified Sun-Canopy-Sensor Topographic Correction (SCS-TC) method described by Soenen et al. (2005) and implemented in GEE by Poortinga et al. (2019). In addition, a bidirectional reflectance distribution function (BRDF) correction was applied to account for differences in solar and viewing angles between sensors. This correction, which adjusts reflectance according to variations in illumination and viewing angle, is based on the MODIS BRDF-based c-factor model—developed for Landsat and using fixed coefficients validated for these sensors (Roy et al., 2016; Zhang et al., 2018), which was implemented in GEE by Poortinga et al. (2019). Finally, the last step was to convert the narrowband albedo (discrete bands) to broadband albedo, that is, the total reflectance in all directions, either in the visible bands (wavelengths from 0.380 to 0.760 μm) or in the shortwave spectral bands (0.250–2.5 μm). We applied the Liang albedo algorithm (Liang, 2001), which considers the green, red, near-infrared (NIR), shortwave IR1 (SWIR1), and shortwave IR2 (SWIR2) bands of the Landsat 8 OLI sensors and Landsat 7 ETM+. Although this algorithm was originally developed for ETM+, it has also been successfully applied to Landsat 8 data proposed by both Naegeli et al. (2017) and Traversa et al. (2021) for use in the presence of ice and snow. The equation for this conversion is as follows:

$$\alpha_{\text{Liang } L8} = 0.356\rho b_{\text{Green}} + 0.130\rho b_{\text{Red}} + 0.373\rho b_{\text{NIR}} + 0.085\rho b_{\text{SWIR1}} + 0.072\rho b_{\text{SWIR2}} - 0.0018 \quad (4)$$

where ρb_x is the surface reflectance in band x. The main advantage of this algorithm is that it considers contributions from a wider range of the spectrum than other algorithms (Knap et al., 1999; Qu et al., 2015), thereby capturing changes in albedo due to variations in snow grain size, which have a particularly large effect at near-infrared and shortwave infrared wavelengths (Wiscombe & Warren, 1980).

2.2.3. Validation of Satellite-Derived Albedo

To validate the albedo data obtained from the Landsat images, a comparison was made with ground measurements from the pyranometers installed on the flux towers at the reservoir and forest sites. This comparison considered the specific footprint of each tower and was carefully synchronized with the satellite overpass times. Both root mean square error (RMSE) and mean absolute error (MAE) were used to evaluate the accuracy of the estimated values.

At each flux tower, two pyranometers, one pointing upward to measure the incident radiation and the other pointing downward to measure the solar radiation reflected by the surface, were used to measure the surface albedo every half hour.

For consistency, half-hourly albedo measurements were averaged over from 10:00 to 14:00 to coincide with the Landsat satellite overpass time. The ground-facing pyranometers have a 150° field of view, while the sky-facing pyranometers have a 180° field of view. They are placed at a height of 2 m above the water level for the reservoir station, above the maximum water level for the shore station, and 24 m above the ground (about 9 m above the tree crowns) for the forest station. Therefore, their respective impact radii are estimated to be approximately 8 m for the reservoir station, 30 m for the shore station, and approximately 90 m for the forest station. The influence radii of the reservoir and shore stations do not exceed 30 m, so the single pixels containing each station were used for comparison. For the forest station, due to its larger influence radius, the weighted average of albedo values was calculated using all pixels within a 90-m radius circular window centered on the station.

This comparison covers the period from June 2018 to October 2023, during which both in situ and satellite data were available. Since the reservoir flux tower is not operational during the winter, a continuous annual time series of water surface radiation had to be constructed. From June to October, data from the reservoir flux tower were used, while during periods of ice cover, radiation measurements were taken from the shore station, assuming equivalent surface conditions between the shore and reservoir. During transition periods (ice breakup: late April to early June; ice freezeup: late October to December), albedo was estimated using the method described by Patel and Rix (2019), which involves modeling the albedo of the water surface as a function of the angle of incidence of the sun and the spectral and angular variations of the reflection, influenced by weather conditions and the water surface.

For the rest of this study, we distinguished between two main conditions based on the presence or absence of snow/ice. This distinction was based on the observation of regional climatic conditions and albedo measurements obtained from towers and satellite data. Thus, snow or ice was generally absent from May to November and present during the rest of the year.

In this article, albedo values for transitional periods, such as snowmelt and the beginning of snowfall, were not considered due to a lack of sufficiently frequent and usable satellite imagery for these phases. However, we recommend that these data be included in future studies in order to enrich the analysis and improve the results for these periods.

2.2.4. Determination of Surface Temperature Using Landsat Imagery

This study uses the Landsat 7 (LANDSAT/LE07/C01/T1) and Landsat 8 (LANDSAT/LC08/C01/T1) data sets available on the GEE platform to determine surface temperature (T_s) after preprocessing the raw reflectance data.

The algorithm resampled the resolution of the thermal bands (100 m for Landsat 8 TIRS and 60 m for band 6 of Landsat 7 ETM+) to 30 m. Due to calibration errors in Band 11 caused by scattered light (Montanaro et al., 2014), only Landsat 8 band 10 was used for surface temperature estimation. These bands were subsequently converted into brightness temperature (BT) using the following two steps (Walawender et al., 2014):

1. Satellite-based digital numbers (DN) were converted to at-sensor spectral radiance ($L\lambda$) using the following equation:

$$L\lambda = (\mathrm{ML} \times Q_{\mathrm{cal}}) + \mathrm{AL} \quad (5)$$

where ML and AL are the band-specific multiplicative and additive rescaling factors obtained from the data set metadata, respectively, and Q_{cal} is the quantized and calibrated standard product DN value of the pixel.

The at-sensor spectral radiances were then converted to BT using metadata and the following equation:

$$\mathrm{BT} = \frac{K_2}{ln\left[\left(\frac{K_1}{L\lambda}\right) + 1\right]} - 273.15 \quad (6)$$

where K_1 and K_2 are the coefficients associated with TIRS Bands 10 for Landsat 8 and with TIRS Band 6 for Landsat 7, found in the metadata file associated with the satellite image, and $L\lambda$ is the spectral radiance at the sensor.

2. The final step is to calculate T_s using BT and emissivity using the following equation (Stathopoulou & Cartalis, 2007):

$$T_s = \frac{\mathrm{BT}}{1 + \left(\frac{\lambda \cdot \mathrm{BT}}{\rho}\right) \ln \varepsilon} \quad (7)$$

where λ is the sensor-specific central wavelength of TIRS, ρ is $hc/\sigma = 1.438 \times 10^{-2}$ m K (h is Planck's constant, c is the speed of light in a vacuum, and σ is the Boltzmann constant), and ε represents the land surface emissivity. The emissivity values used were 0.98 for conifers and 0.95 for water and snow, following Moene and Dam (2014). Since the vegetation fraction can vary from pixel to pixel, the emissivity of the forest was adjusted according to the vegetation fraction of each pixel, determined from the normalized difference vegetation index (NDVI) derived from Landsat 7 and 8. Equations for calculating NDVI, vegetation fraction, and emissivity can be found in Ermida et al. (2020), Meng et al. (2019), Salih et al. (2018), and Stathopoulou and Cartalis (2007). Surface temperatures derived from satellite imagery were validated by comparison with measurements from the three flux stations of the study area, using the same methodology as for the validation of albedo with in situ observations. These in situ temperatures were estimated from the rising infrared radiation measured by pyrgeometers using the Stefan-Boltzmann equation and assuming a constant emissivity identical to that used in the previous treatments. After validation, weekly averages of surface temperatures were calculated for the periods before and after the impoundment of the reservoir. To fill gaps in the weekly satellite surface temperature data, in situ measurements from pyrgeometers were used where available. Otherwise, satellite temperatures were temporally interpolated. Finally, polynomial regression was applied to the weekly series to better represent the temporal variation of surface temperatures and to refine the analysis of their seasonal dynamics.

2.3. Total Net Radiation

The total net radiation was calculated using Equations 1–3. In this study, the variables α and T_s are derived from Landsat 7 and Landsat 8 data, while the incident shortwave and longwave radiation are taken from the ERA5-Land reanalysis (Hersbach et al., 2020) for the period 2000–2023. However, due to the low spatial resolution of the reanalysis data (~9 km), errors may occur in the estimation of incoming radiation at the local scale. To correct for these errors, we compared ERA5-Land reanalysis data with direct measurements of solar and infrared radiation from the three flux stations, for the period 2018–2023. The discrepancies between the reanalysis values and the in situ measurements were calculated. These discrepancies were then applied to the entire study period (2000–2023) by adding or subtracting the observed discrepancies, depending on their sign. These adjustments made it possible to improve the accuracy of the estimates of shortwave and infrared solar radiation, making them more appropriate to local conditions and reducing the impact of errors caused by the low spatial resolution of the reanalysis data.

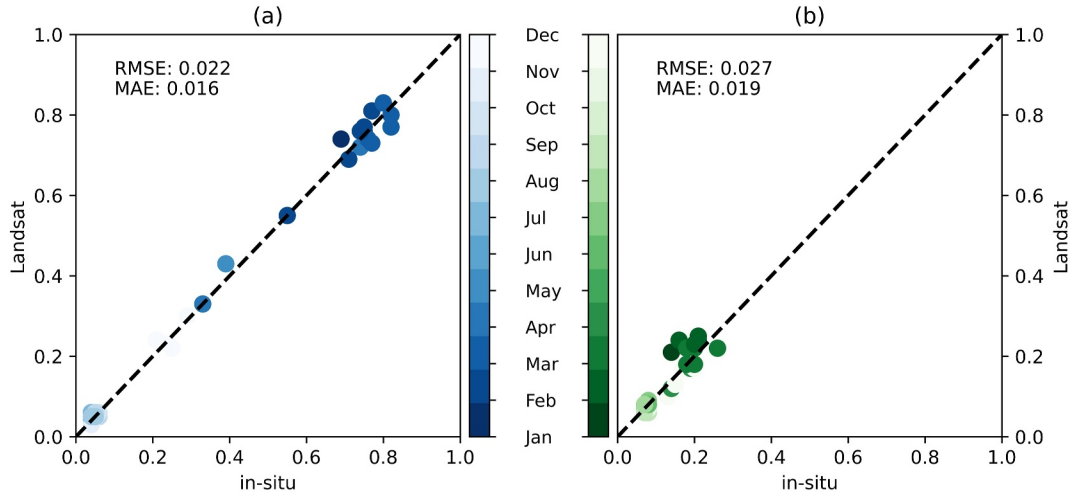

Figure 2. Comparison between satellite retrievals and ground measurements of albedo: (a) reservoir, (b) forest.

3. Results and Discussion

3.1. Satellite Derived Surface Albedo

The Landsat surface albedo values have been validated based on satellite overpass times and the radius of influence of each tower. The Landsat database allowed the generation of 104 albedo maps for the study period.

3.1.1. Validation of Satellite-Derived Albedo

Validation was performed using 36 dates from June 2018 to October 2023. As shown in Figure 2, the comparison of the Landsat albedo with that measured by the reservoir station resulted in RMSE of 0.022 (RRMSE in situ: 6.35%, RRMSE Landsat: 6.29%) and a bias of 0.016. Similarly, an RMSE of 0.027 (RRMSE in situ: 20.33%, RRMSE Landsat: 19.73%) and a bias of 0.019 were obtained from the comparison with the forest station albedo, also shown in Figure 2. This level of accuracy was considered sufficient to confirm the validity of albedo estimates based on Landsat data and related algorithms, both in the absence and presence of snow and ice, since satellite and ground instruments do not cover exactly the same surfaces.

3.1.2. Evolution of Albedo Around the Reservoir Filling Period

Figure 3 compares the variation of the mean albedo of pixels located within the reservoir boundary (red contour in Figure 1b) before (green) and after (blue) the installation of the hydroelectric reservoir as a function of Julian day for different Landsat dates. This average was calculated over all pixels corresponding to the reservoir area, using the same delineation before and after installation for both periods. Figures 4 and 5 illustrate the spatial variation of albedo across the reservoir during winter, summer, and transition periods, such as the onset and melting of the ice and snow.

Before the reservoir was impounded, when forest dominated the site, the mean summer albedo was 0.08 ± 0.002, which is typical of a snow-free coniferous forest (Betts & Ball, 1997). At the beginning of winter (mid-November/early December to around mid-January), when the first snow falls, the albedo increases to values between 0.10 and 0.15. The first snowfall gradually covers the ground and trees, gradually increasing the albedo. In winter (mid-January to mid-April), the average albedo reached its maximum, with values around 0.25 ± 0.02. These values indicate that snow remained on tree crowns only for a short period immediately following snowfall. Snow in the subcanopy has less of an effect on the overall reflectivity of the surface than if it were visible from above, for example, by covering tree branches (Kuusinen et al., 2012). Under snowy conditions, the albedo of wooded areas varies according to the leaf area index (LAI) of the forest (Manninen & Jääskeläinen, 2018). Intercepted snow in the forest canopy increases the albedo by about 20% compared to (canopy) snow-free conditions (Kuusinen et al., 2012). During the snowmelt period (mid-April to early June), mean albedo values decreased and varied between 0.11 and 0.15 depending on the amount of snow intercepted by the canopy and on the ground.

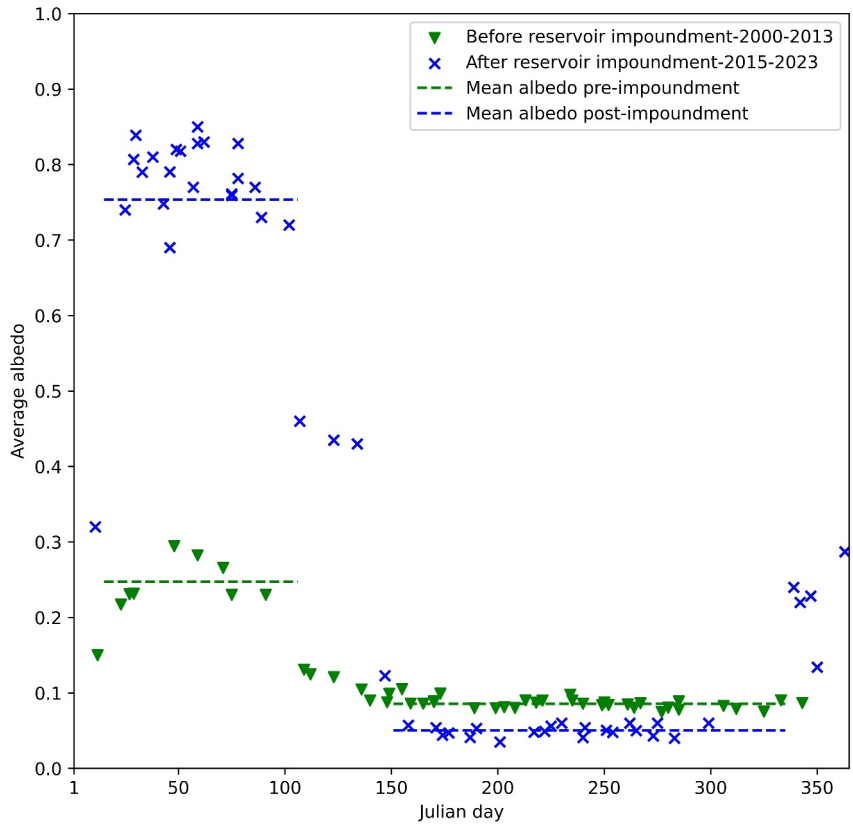

Figure 3. Landsat albedo values before and after the reservoir impoundment.

These values are typical for boreal forests during the snowmelt season (Jääskeläinen & Manninen, 2021). As snow melts, natural debris such as needles, branches, and moss accumulate on its surface, lowering its albedo. This effect is amplified because wet snow naturally has a lower albedo than dry snow.

As shown in Figure 6, analysis of snow depth data under the canopy and in the gaps between 2021 and 2023 shows that snow accumulation generally begins in mid-November. Snow depths are systematically higher in the gaps, with a difference of up to 50 cm between the two zones. The snow started to melt between mid-April and the end of May, and the snow under the trees melted about 2 weeks before the snow in the gaps. These observations reveal the significant influence of the presence and duration of snow cover on temporal variations in albedo. In forest gaps, winter albedo is generally higher than under the canopy. Once the snowpack exceeds a certain depth threshold, however, further accumulation has little additional effect on albedo. The higher values observed in gaps primarily reflect the presence of a continuous reflective surface and the addition of fresh snow, which has an intrinsically higher albedo. Under the canopy, albedo is reduced by the rapid contamination of the understory snowpack from litterfall and by the substantial proportion of snow-free canopy elements within the field of view. In addition, the early melting of snow under trees reduces the length of time that snow contributes to surface albedo, thus influencing its seasonal variations. In addition, the early melting of snow under trees reduces the length of time that snow contributes to surface albedo, thus influencing its seasonal variations.

After the impoundment, the albedo decreased to approximately 0.05 ± 0.003 during the ice-free period, which is typical for open water conditions (Ponce et al., 1997; Wohlfahrt et al., 2021). These low values are primarily caused by the presence of water, whose surface absorbs more solar radiation than ice, snow, or vegetation. At the beginning of winter, the average albedo of the reservoir reached values above 0.25. On 13 December 2015, as shown in Figure 5, the reservoir is not completely covered by snow and some pixels show a mixture of water surfaces, clear ice, and fresh snow. These heterogeneous values result from incomplete ice and snow cover and from variations in the density and composition of the snow present. In winter, when the reservoir was completely covered with ice and snow, the albedo reached values of between around 0.70 and 0.90, with a mean of 0.77 ± 0.04. This substantial

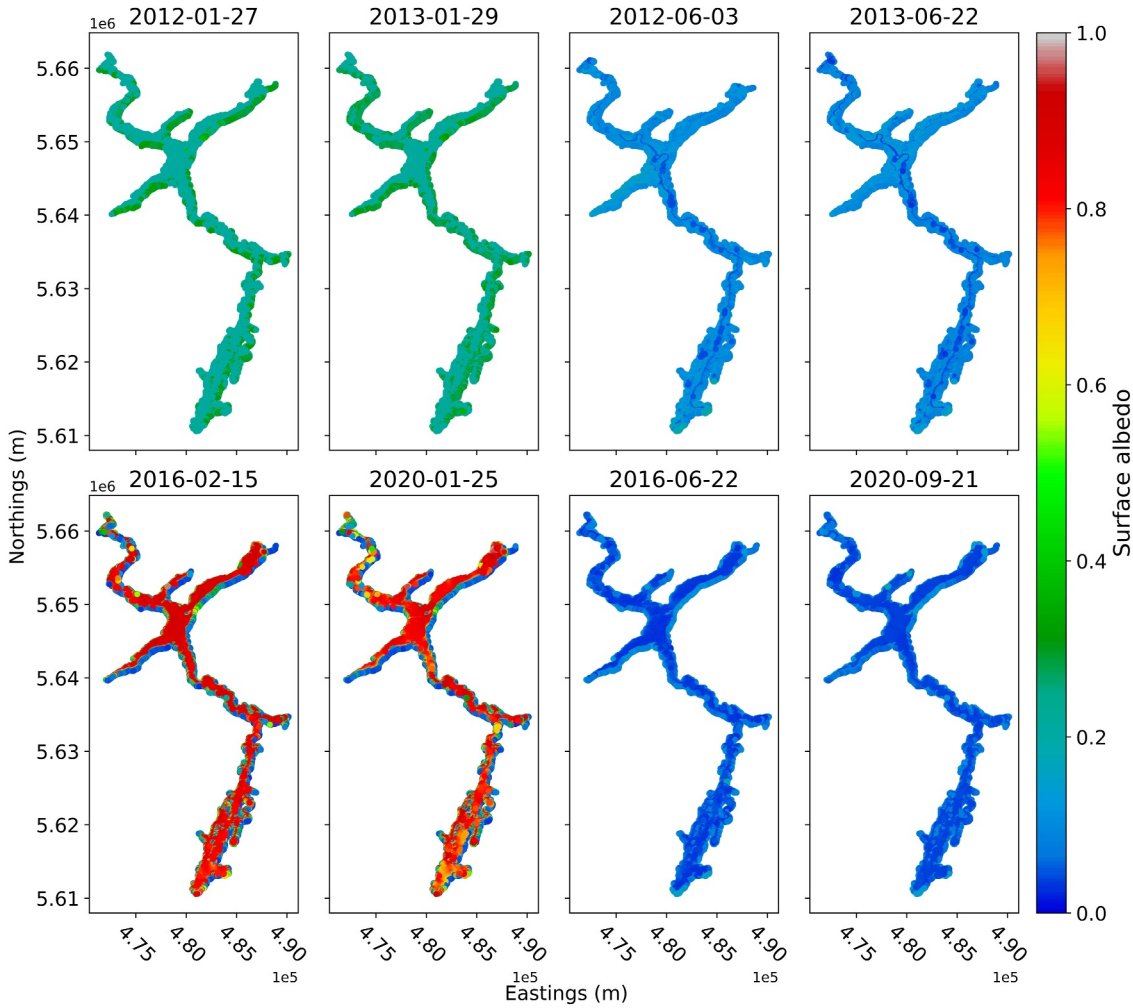

Figure 4. Typical winter (first two columns) and summer (last two columns) Landsat albedo values before (top row) and after (bottom row) reservoir impoundment.

increase is due to the high reflectivity of undisturbed snow on the reservoir. Typically, the broadband reflectivity of pure snow in midwinter is around 0.83 (Hall, 2012; Warren, 1982; Wiscombe & Warren, 1980). During the snowmelt period (mid-April to early June), the surface albedo tends to decrease while remaining quite high, fluctuating on average around 0.4. For example, looking at 17 April 2021, in Figure 5, we can see a heterogeneity of albedo values, with some pixels around 0.4, typical of clear ice, and other pixels showing values around 0.2, typical of dirty ice (Hall, 2012). Before impoundment, the mean albedo in the presence of snow/ice was around 0.25. After impoundment, under the same conditions, the average albedo rose to 0.77. During the snow-free months, the average albedo before impoundment was 0.08, then decreased to 0.05 after impoundment.

3.2. Land Surface Temperature Retrieval

As shown in Figure 7, the comparative analysis of surface temperatures between satellite imagery and flux tower measurements covering the period from June 2018 to October 2023 revealed an RMSE of 3.39°C for the reservoir station and an RMSE of 2.95°C for the forest station. These values are consistent with the uncertainties reported in previous studies, which typically range between 0.5 and 3°C (Duan et al., 2021; Guo et al., 2020; Laraby & Schott, 2018; Wang et al., 2019). Therefore, our results can be considered sufficiently reliable to validate the satellite-derived observations, even under the particular conditions of a boreal environment characterized by recurring snow cover.

Figure 8a shows the variations in weekly mean surface temperatures before and after reservoir installation, following the application of a polynomial regression to smooth the signal. This regression yielded high R^2 values

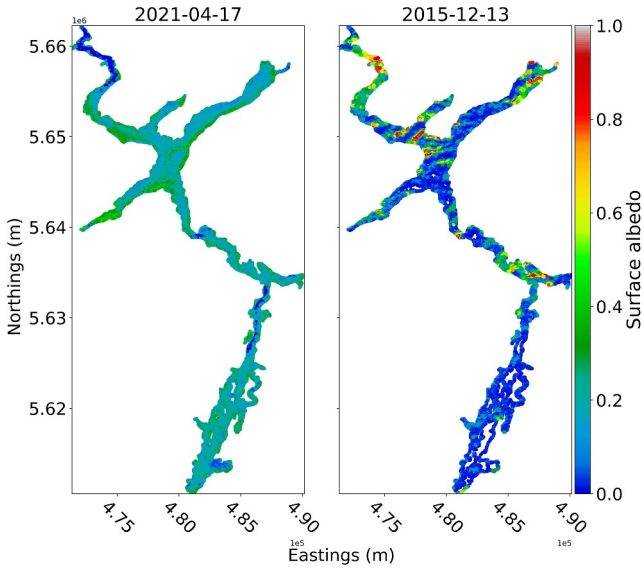

Figure 5. Examples of the Landsat albedo at ice-on (left) and ice-off (right) transitions dates, both after reservoir impoundment.

of 0.96 and 0.94 for the periods before and after reservoir installation, along with RMSE of 2.02 and 2.74°C, respectively.

According to the observations in Figure 8a, during the first 10 weeks of winter, the surface temperatures after the installation of the reservoir were slightly higher than those before the installation, when the forest dominated land cover at the site, with an average amplitude difference varying between 2 and 7°C. The forest reached its minimum temperature about 3 weeks before the reservoir, with a minimum of −17°C around Week 6, while the reservoir reached a minimum of −14°C around Week 9. As spring and summer approach, the forest gradually warmed up before the reservoir, with temperatures between 1 and 5°C higher. Between June and August, the forest reached a peak of about 17°C around Week 30, while the reservoir reached a peak of 16°C 5 weeks later (Week 35). As autumn approaches, the forest begun to cool down before the reservoir from Week 35, with temperatures lower than those in the reservoir, with an amplitude difference of about 1–5°C. Overall, the forest showed greater thermal amplitudes in spring and summer, and lower ones in autumn and winter, with temperature peaks lagging 3–5 weeks behind those of the reservoir. An analysis of weekly air temperatures from ERA5 reanalysis was also conducted for the periods before and after impoundment. The results show broadly similar temporal patterns for both periods, confirming that the observed differences in surface temperatures are predominantly due to the reservoir effect rather than interannual climate variability (Figure 8b).

The analysis of variations in reservoir surface temperatures complements the findings of Kallel et al. (2024). In their study, they examined the thermal regime of this reservoir over the period 2018–2023, highlighting the dimictic nature of the reservoir. Their results showed that surface temperatures peak in August. As the ambient air cools as autumn approaches, surface temperatures decrease, leading to the formation of a seasonal winter ice layer, occasionally covered by snow. In the spring, this ice layer melts, and surface temperatures rise again.

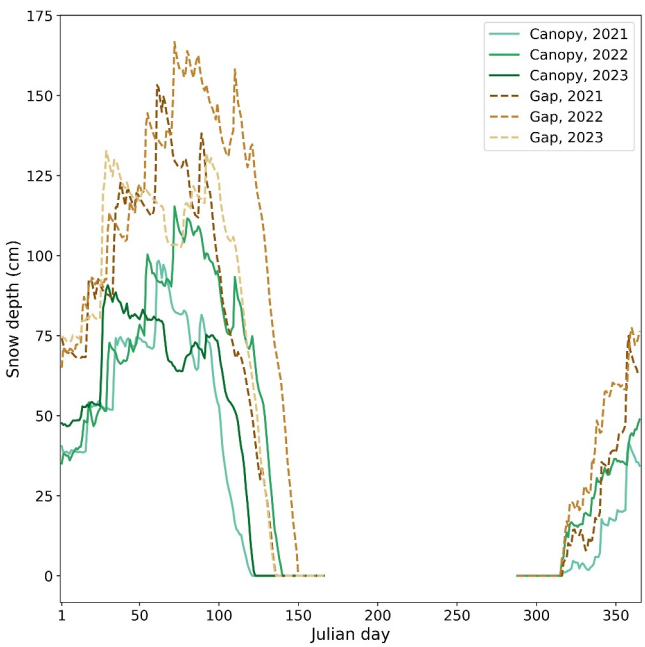

Figure 6. Temporal variation in snow depth under the canopy and in forest gaps, from 2021 to 2023.

The temperature difference between the two environments (forest and reservoir) can be explained by their distinct thermal properties and specific responses to seasonal variations. Due to its large water mass, the reservoir has a high thermal inertia, meaning it takes longer to adjust its temperature than the forest. Thus, even when the reservoir begins to cool, it generally maintains higher temperatures over a longer period than the forest. These results complement the findings of other studies that have also highlighted the significant impact of the thermal characteristics of water bodies on seasonal temperature variations. Indeed, many studies under higher-latitude regions (e.g., Dutra et al., 2010; Eaton et al., 2001; Nordbo et al., 2011; Samuelsson et al., 2010; Subin et al., 2012) have highlighted that lakes and reservoirs absorb heat in summer and partially release it in autumn, thereby attenuating diurnal and annual temperature variations.

3.3. Estimation of the Net Radiation

Figure 9a shows the weekly average values of the estimated net shortwave radiation from 2000 to 2023, differentiating before (2000–2013, in green) and after (2015–2023, in blue) the impoundment. During the first 17 weeks of the year, the net shortwave radiation of the area dominated by forest exceeds that of the reservoir, with a difference in amplitude ranging from 30 to 160 W m^{-2}, increasing from 43 to 233 W m^{-2} by week 17, while that of the reservoir ranges from 11 to 74 W m^{-2}. This difference can be attributed to the lower winter albedo of the forest, which increases solar absorption, especially as the tree canopy is not completely covered by snow, unlike the reservoir.

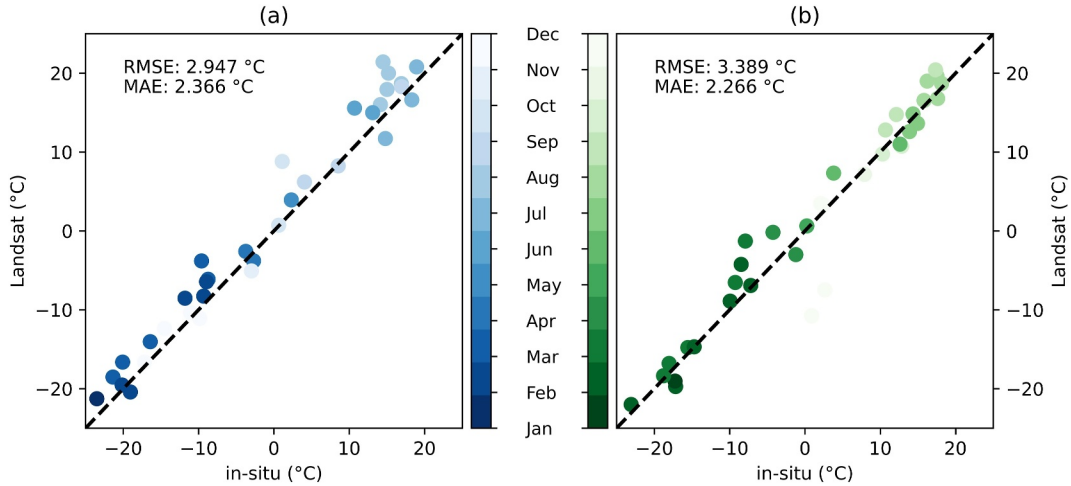

Figure 7. Comparison between surface temperature ground measurements and satellite retrievals: (a) reservoir, (b) forest.

Between Weeks 17 and 34, which generally correspond to spring (snowmelt period) and summer, the reservoir had slightly higher net shortwave radiation, with an amplitude difference of around 15 W m^{-2}, peaking at 335 W m^{-2} for the reservoir compared to 319 W m^{-2} for the forest. This could be due to the lower albedo of the water in the reservoir during the open water period, resulting in increased solar absorption. As late summer and fall approach, both net shortwave radiation values gradually decreased, with a return to higher net shortwave radiation for the forest from Week 49, as the reservoir is transitioning toward winter conditions.

The average weekly variation of the net longwave radiation observed between 2000 and 2023, illustrated in Figure 9b, shows negative values, since the incoming longwave radiation is lower than that emitted by the surface. During the first 10 weeks, the longwave radiation from the forest exceeded that from the reservoir, with a maximum difference of 20 W m^{-2}. This can be explained by the higher surface temperatures of the reservoir compared to the forest during this period, as shown in Section 3.2. Then, with the arrival of spring and during the summer, until about Week 35, the longwave radiation from the reservoir exceeds that from the forest, with a maximum difference of 40 W m^{-2}. From Week 35, as the summer begun to fade and autumn approaches, the forest vegetation regained its influence, producing a maximum difference of around 35 W m^{-2} compared to the reservoir.

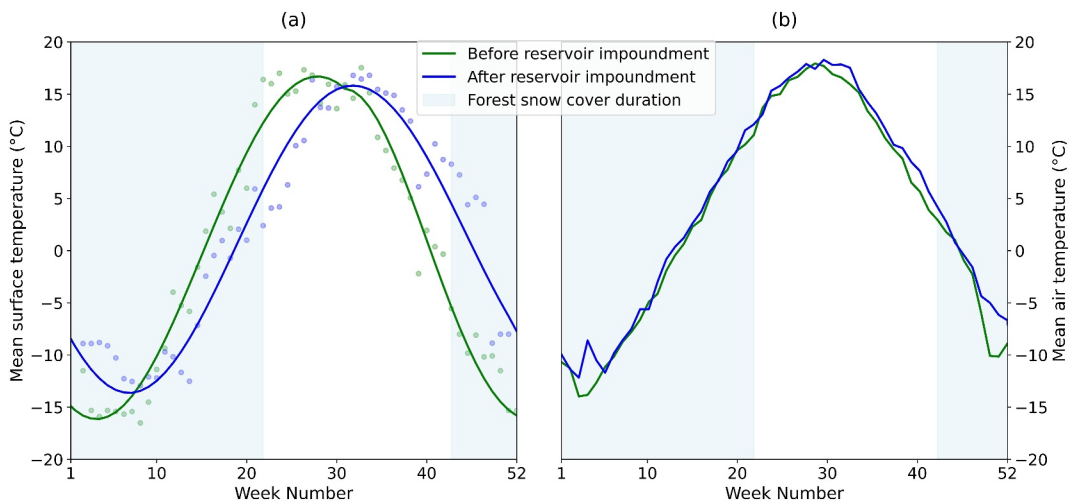

Figure 8. Temporal variations in (a) average weekly surface temperatures and (b) average weekly air temperatures before and after reservoir impoundment.

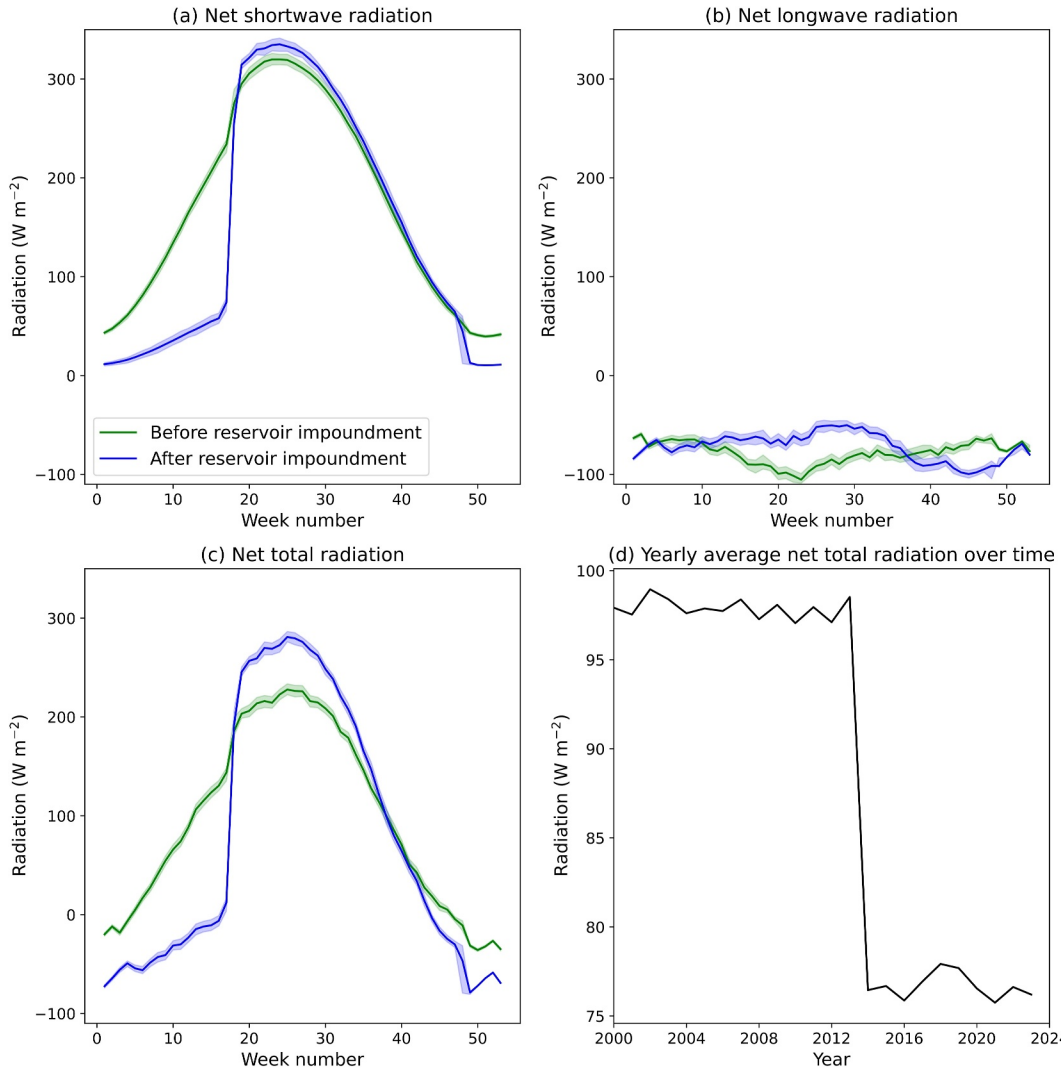

Figure 9. (a) Weekly average shortwave radiation, (b) weekly average longwave radiation, and (c) weekly average total net radiation before and after reservoir impoundment over the years (2000–2023), with the quantiles (25th and 75th percentiles) represented by colored bands. (d) Yearly average net radiation over the period (2000–2023).

An examination of the net radiation balance, resulting from the addition of net shortwave and longwave radiation, as shown in Figure 9c, reveals significant differences between the forest and the reservoir. During Weeks 1–17 of the winter season, the total net radiation from the forest systematically exceeded that from the reservoir, by 60 up to 140 W m^{-2}. Net radiation values from the forest range from −25 to 138 W m^{-2} and show a positive trend with time. In contrast, variation in the net radiation from the reservoir remains relatively low, fluctuating between −86 and −3 W m^{-2}.

As spring approaches and during the summer, the total net radiation from the reservoir increased again, with differences relative to the forest between 5 and 50 W m^{-2}. In autumn and at the end of the year, both curves gradually decrease. In the last week of the year, the net radiation from the reservoir reached −82 W m^{-2}, while that from the forest followed a similar downward trend, stabilizing at about −40 W m^{-2}.

The interannual variability of the net radiation is illustrated in Figures 9a–9c by a light-colored band representing the 25th and 75th quantiles of the distribution of weekly values. These bands reveal that the interannual variability is small in comparison with the seasonal variability.

On an annual basis, the net total radiation shows subtle variations over the preimpoundment (2000–2013), with values oscillating around 97.9 ± 0.5 W m^{-2}, as shown in Figure 9d. However, during the postimpoundment

period (2015 onward), there is a significant shift, as the average total net radiation drops to around 76.7 ± 0.7 W m^{-2}. This suggests a noticeable cooling effect due to the damming of the reservoir, which caused a reduction of about 21.2 W m^{-2} compared to the preimpoundment period. Figure 9a indicates that the cooling effect is particularly pronounced in winter, when snow completely covers the reservoir, due to its high albedo. On the other hand, in the absence of snow, a slight warming is observed, but this is small compared with the winter cooling. Figure 9d also suggests that the interannual variability is much smaller than the documented effect of the reservoir impoundment.

Results presented here indicate that the installation of the Romaine-2 hydroelectric reservoir (50.69°N) has a significant cooling impact on the local net radiation, as anticipated by Wohlfahrt et al. (2021) for reservoirs located above 44°N, with notable seasonal variations in both short and long wavelengths. These variations reflect the differences between the preimpoundment surface conditions (forested areas) and those of the reservoir, highlighting the importance of hydroelectric projects on the local radiative balance in both the short and long term. Changes in albedo and surface temperature can influence the local radiative balance, potentially affecting the regional climate and surrounding ecosystems.

3.4. Study Limitations and Future Perspectives

Although this study provides solid results, it has certain limitations that, although they do not significantly alter the conclusions, could provide avenues for improvement in future research. Firstly, the analysis did not explore the evolution of albedo values during the transitional periods, particularly those for the year 2014, the key moment when water retention in the reservoir began and its maximum level was reached. Another limitation is the lack of data on albedo values during periods of snowmelt and the onset of snow accumulation. Including hese data, obtained using complementary approaches, would help refine the assessment of seasonal variations and the overall impact of albedo on annual net radiation. In addition, a detailed analysis of the variations of the reservoir level over the year and of the zones directly exposed to climatic conditions would enrich the results. These elements, influenced by climate and reservoir management, will contribute to a better understanding of the spatial and temporal evolution of the reservoir. Finally, an assessment of the impact of reservoir impoundment on the radiative balance of adjacent forests would provide an enriching perspective on the ecological consequences of this water management and strengthen our understanding of the interactions between the reservoir and its surrounding ecosystem.

4. Conclusion

This study presented an integrative approach that combined satellite data analysis, meteorological reanalyses, and in situ measurements to assess the impact of a hydroelectric reservoir impoundment in the subarctic on the local radiative balance. Spatial and temporal variations in albedo and surface temperature were analyzed using data from the Landsat 7 ETM+ and Landsat 8 OLI/TIRS satellites on 104 dates between 2000 and 2023. By integrating these data with ERA5-Land reanalysis and in situ measurements, we evaluated the combined effects of albedo and temperature changes on shortwave and longwave radiative fluxes.

Reservoir impoundment induced substantial changes in surface properties: winter albedo increased from 0.25 ± 0.02 to 0.7–0.9, while summer albedo decreased from 0.08 ± 0.002 to 0.05 ± 0.003. Seasonal surface temperatures also shifted, with winters becoming 2–7°C warmer, summers 1–5°C cooler, and the seasonal temperature maximum delayed by 3–5 weeks. Over the 2000–2023 period, these effects yielded a net annual cooling of 21.2 W m^{-2}, primarily driven by the strong winter radiative response, which partially offset summer warming. These results demonstrate that hydroelectric reservoirs can exert complex, seasonally dependent effects on local climate.

More broadly, our findings underscore that the radiative consequences of land-cover change are not unidirectional but emerge from the net balance of competing seasonal forcings. By evaluating both shortwave (albedo-driven) and longwave (temperature-driven) radiative fluxes concurrently, our study provides a comprehensive assessment of the surface energy balance and underscores the critical importance of incorporating these radiative and thermal feedbacks into regional energy balance assessments and local climate projections. We emphasize that these findings are specific to a subarctic environment with seasonal snow cover, where the winter albedo effect is dominant, and should not be extrapolated to other climates. Nevertheless, the principle that seasonal asymmetry governs the net radiative impact of land use change is widely applicable.

The methodological framework developed here provides a generalizable approach for studying other reservoirs and anthropogenic land-cover conversions, offering a valuable tool for energy planning and for anticipating their climatic impacts. This work establishes a foundation for further research on the combined effects of albedo, surface temperature, and radiative fluxes on regional climate, contributing to more effective, evidence-based strategies for climate management and mitigation.

Appendix A

Table A1
Spectral Band Specifications for Landsat Sensors ETM+, OLI, and TIRS

Band (μm)	Landsat 8 OLI and TIR	Landsat 7 ETM+
Blue	0.45–0.51	0.44–0.51
Green	0.53–0.59	0.52–0.60
Red	0.64–0.67	0.63–0.69
Near-infrared (NIR)	0.85–0.88	0.77–0.90
Shortwave Infrared 1	1.57–1.65	1.55–1.75
Shortwave Infrared 2	2.11–2.29	2.06–2.34
Panchromatic	0.50–0.68	0.51–0.89
Thermal Infrared (TIR 1)	10.60–11.19	1.03–12.36
Thermal Infrared 2 (TIR2)	11.50–12.51	–

Table A2
List of Images Used for 2000–2023

Date	Platform	Percentage cloud coverage (%)
2000-06-18	Landsat 7	7
2001-01-12	Landsat 7	9
2001-05-20	Landsat 7	5
2001-09-09	Landsat 7	3
2004-06-13	Landsat 7	28
2005-01-23	Landsat 7	1
2005-03-12	Landsat 7	2
2005-07-18	Landsat 7	29
2005-12-09	Landsat 7	19
2006-06-19	Landsat 7	29
2006-08-06	Landsat 7	15
2006-08-22	Landsat 7	16
2006-09-07	Landsat 7	3
2007-04-19	Landsat 7	12
2007-08-09	Landsat 7	9
2007-10-12	Landsat 7	29
2008-02-17	Landsat 7	2
2008-04-21	Landsat 7	1
2008-07-26	Landsat 7	24
2008-08-27	Landsat 7	6
2008-09-05	Landsat 7	0
2009-11-02	Landsat 7	2

Table A2
Continued

Date	Platform	Percentage cloud coverage (%)
2010-05-29	Landsat 7	1
2010-08-01	Landsat 7	7
2010-09-18	Landsat 7	10
2010-10-04	Landsat 7	0
2010-11-21	Landsat 7	26
2011-05-16	Landsat 7	6
2011-09-21	Landsat 7	29
2011-10-07	Landsat 7	26
2011-11-08	Landsat 7	18
2012-01-27	Landsat 7	2
2012-02-28	Landsat 7	8
2012-03-15	Landsat 7	8
2012-03-31	Landsat 7	4
2012-05-02	Landsat 7	11
2012-05-27	Landsat 7	6
2012-06-03	Landsat 7	3
2012-07-21	Landsat 7	1
2012-08-22	Landsat 7	18
2012-09-23	Landsat 7	11
2013-01-29	Landsat 7	0
2013-06-22	Landsat 7	0
2013-07-08	Landsat 7	5
2013-10-12	Landsat 7	0
2013-11-29	Landsat 7	9
2014-01-08	Landsat 8	14
2014-01-24	Landsat 8	0
2014-02-09	Landsat 8	2
2014-09-05	Landsat 8	3
2014-10-07	Landsat 8	3
2014-10-23	Landsat 8	0
2015-01-11	Landsat 8	3
2015-02-28	Landsat 8	3
2015-03-16	Landsat 8	5
2015-05-03	Landsat 8	19
2015-06-20	Landsat 8	2
2015-09-08	Landsat 8	21
2015-12-13	Landsat 8	3
2016-01-30	Landsat 8	0
2016-02-15	Landsat 8	1
2016-03-18	Landsat 8	0
2016-06-22	Landsat 8	27
2016-07-08	Landsat 8	2
2017-08-28	Landsat 8	0

Table A2
Continued

Date	Platform	Percentage cloud coverage (%)
2018-01-19	Landsat 8	0
2018-02-20	Landsat 8	0
2018-05-27	Landsat 8	1
2018-10-02	Landsat 8	18
2018-12-05	Landsat 8	1
2019-02-07	Landsat 8	29
2019-03-27	Landsat 8	4
2019-04-12	Landsat 8	2
2019-05-14	Landsat 8	0
2019-08-18	Landsat 8	7
2019-09-19	Landsat 8	0
2019-12-08	Landsat 8	1
2019-12-24	Landsat 8	7
2020-01-25	Landsat 8	2
2020-02-26	Landsat 8	0
2020-03-29	Landsat 8	3
2020-07-19	Landsat 8	26
2020-08-04	Landsat 8	1
2020-09-21	Landsat 8	1
2021-02-28	Landsat 8	15
2021-03-16	Landsat 8	0
2021-04-17	Landsat 8	1
2021-07-06	Landsat 8	1
2021-10-10	Landsat 8	29
2021-10-26	Landsat 8	29
2021-12-29	Landsat 8	5
2022-02-15	Landsat 8	4
2022-03-03	Landsat 8	9
2022-03-19	Landsat 8	0
2022-06-07	Landsat 8	2
2022-08-10	Landsat 8	21
2022-09-11	Landsat 8	2
2023-02-02	Landsat 8	4
2023-02-18	Landsat 8	10
2023-06-26	Landsat 8	18
2023-08-13	Landsat 8	19
2023-08-29	Landsat 8	15
2023-09-30	Landsat 8	10
2023-12-16	Landsat 8	16

Conflict of Interest

The authors declare no conflicts of interest relevant to this study.

Data Availability Statement

The albedo and surface temperature data used in this study were derived from Landsat 7 ETM+ and Landsat 8 OLI/TIRS satellite images, accessed via the Google Earth Engine (GEE) platform (Gorelick et al., 2017). Shortwave (SW) and longwave (LW) radiation data were obtained from the ERA5-Land reanalysis data set covering the period 2000–2023 (Hersbach et al., 2020). In situ measurements of shortwave and longwave radiation were collected using pyranometers and pyrgeometers installed on three flux towers within the study area (Ben Aba et al., 2025). Snow depth measurements were recorded using ultrasonic sensors (Judd Communications and SR50 models) (Ben Aba et al., 2025). Data and Python scripts used to generate figures are available at the following repository (Ben Aba et al., 2025).

Acknowledgments

This work was supported by the Natural Sciences and Engineering Research Council of Canada (NSERC) through Grants ALLRP-549108-19 and RGPIN-2020-04286. Additional funding was obtained from NSERC and Hydro-Québec through the Alliance program (Grant ALLRP-587030-23, "Impact of hydroelectricity in cold regions in the face of a changing cryosphere—the case of the Romaine complex"). Further support was provided by the Québec Ministère des Ressources naturelles et des Forêts (Project 142332139) and a Marthe-et-Robert-Ménard doctoral scholarship. The authors would also like to thank Antoine Thiboult, who is responsible for operating and maintaining the flux towers and auxiliary instrumentation.

References

Ben Aba, I., Nadeau, D. F., Sylvain, J.-D., Drolet, G., & Anctil, F. (2025). Estimating the impact of impounding an 85-km^2 hydropower reservoir in a subarctic environment on the local radiation balance (Version 1.0) [Dataset and Software]. *Zenodo*. https://doi.org/10.5281/zenodo.15586972

Betts, A. K., & Ball, J. H. (1997). Albedo over the boreal forest. *Journal of Geophysical Research*, *102*(D24), 28901–28909. https://doi.org/10.1029/96JD03876

Canada Energy Regulator. (2024). CER—Provincial and territorial energy profiles—Quebec. Retrieved from https://www.cer-rec.gc.ca/en/data-analysis/energy-markets/provincial-territorial-energy-profiles/provincial-territorial-energy-profiles-quebec.html

Duan, S.-B., Li, Z.-L., Zhao, W., Wu, P., Huang, C., Han, X.-J., et al. (2021). Validation of Landsat land surface temperature product in the conterminous United States using in situ measurements from SURFRAD, ARM, and NDBC sites. *International Journal of Digital Earth*, *14*(5), 640–660. https://doi.org/10.1080/17538947.2020.1862319

Dutra, E., Stepanenko, V., Balsamo, G., Viterbo, P., Miranda, P., Mironov, D., & Schaer, C. (2010). An offline study of the impact of lakes on the performance of the ECMWF surface scheme. *Boreal Environment Research*, *15*, 100–112.

Eaton, A. K., Rouse, W. R., Lafleur, P. M., Marsh, P., & Blanken, P. D. (2001). Surface energy balance of the Western and Central Canadian Subarctic: Variations in the energy balance among five major terrain types. *Journal of Climate*, *14*(17), 3692–3703. https://doi.org/10.1175/1520-0442(2001)014<3692:SEBOTW>2.0.CO;2

Ermida, S. L., Soares, P., Mantas, V., Göttsche, F.-M., & Trigo, I. F. (2020). Google Earth engine open-source code for land surface temperature estimation from the Landsat series. *Remote Sensing*, *12*(9), 1471. https://doi.org/10.3390/rs12091471

Gorelick, N., Hancher, M., Dixon, M., Ilyushchenko, S., Thau, D., & Moore, R. (2017). Google Earth engine: Planetary-scale geospatial analysis for everyone. *Remote Sensing of Environment*, *202*, 18–27. https://doi.org/10.1016/j.rse.2017.06.031

Guo, J., Ren, H., Zheng, Y., Lu, S., & Dong, J. (2020). Evaluation of land surface temperature retrieval from Landsat 8/TIRS images before and after stray light correction using the SURFRAD dataset. *Remote Sensing*, *12*(6), 1023. https://doi.org/10.3390/rs12061023

Hall, D. (2012). *Remote sensing of ice and snow*. Springer Science & Business Media.

Hansen, M. C., & Loveland, T. R. (2012). A review of large area monitoring of land cover change using Landsat data. *Remote Sensing of Environment*, *122*, 66–74. https://doi.org/10.1016/j.rse.2011.08.024

Hersbach, H., Bell, B., Berrisford, P., Hirahara, S., Horányi, A., Muñoz-Sabater, J., et al. (2020). The ERA5 global reanalysis. *Quarterly Journal of the Royal Meteorological Society*, *146*(730), 1999–2049. https://doi.org/10.1002/qj.3803

Hydro-Québec. (2007). Résumé de l'étude d'impact sur l'environement. In *Complexe de la Romaine: Étude d'impact sur l'environnement* (Vol. 1). Retrieved from https://www.hydroquebec.com/data/romaine/pdf/ei_resume_environnement.pdf

Hydro-Québec. (2024). Centrales—Hydro-Québec production. Retrieved from https://www.hydroquebec.com/production/centrales.html

IEA. (2022). IEA at COP27: The role of hydropower in achieving climate resilience—Event. Retrieved from https://www.iea.org/events/iea-at-cop27-the-role-of-hydropower-in-achieving-climate-resilience

IHA. (2024). 2024 world hydropower outlook: Opportunities to advance net zero. Retrieved from https://www.hydropower.org/publications/2024-world-hydropower-outlook

Irambona, C., Music, B., Nadeau, D. F., Mahdi, T. F., & Strachan, I. B. (2018). Impacts of boreal hydroelectric reservoirs on seasonal climate and precipitation recycling as simulated by the CRCM5: A case study of the La Grande River watershed, Canada. *Theoretical and Applied Climatology*, *131*(3), 1529–1544. https://doi.org/10.1007/s00704-016-2010-8

Irons, J. R., Dwyer, J. L., & Barsi, J. A. (2012). The next Landsat satellite: The Landsat data continuity mission. *Remote Sensing of Environment*, *122*, 11–21. https://doi.org/10.1016/j.rse.2011.08.026

Jääskeläinen, E., & Manninen, T. (2021). The effect of snow at forest floor on boreal forest albedo diurnal and seasonal variation during the melting season. *Cold Regions Science and Technology*, *185*, 103249. https://doi.org/10.1016/j.coldregions.2021.103249

Kallel, H., Thiboult, A., Mackay, M. D., Nadeau, D. F., & Anctil, F. (2024). Modeling heat and water exchanges between the atmosphere and an 85-km^2 dimictic subarctic reservoir using the 1D Canadian Small Lake model. *Journal of Hydrometeorology*, *25*(5), 689–707. https://doi.org/10.1175/JHM-D-22-0132.1

Knap, W. H., Reijmer, C. H., & Oerlemans, J. (1999). Narrowband to broadband conversion of Landsat TM glacier albedos. *International Journal of Remote Sensing*, *20*(10), 2091–2110. https://doi.org/10.1080/014311699212362

Kuusinen, N., Kolari, P., Levula, J., Porcar-Castell, A., Stenberg, P., & Berninger, F. (2012). Seasonal variation in boreal pine forest albedo and effects of canopy snow on forest reflectance. *Agricultural and Forest Meteorology*, *164*, 53–60. https://doi.org/10.1016/j.agrformet.2012.05.009

Laraby, K. G., & Schott, J. R. (2018). Uncertainty estimation method and Landsat 7 global validation for the Landsat surface temperature product. *Remote Sensing of Environment*, *216*, 472–481. https://doi.org/10.1016/j.rse.2018.06.026

Levasseur, A., Mercier-Blais, S., Prairie, Y. T., Tremblay, A., & Turpin, C. (2021). Improving the accuracy of electricity carbon footprint: Estimation of hydroelectric reservoir greenhouse gas emissions. *Renewable and Sustainable Energy Reviews*, *136*, 110433. https://doi.org/10.1016/j.rser.2020.110433

Li, X., Zhou, J., Huang, Y., Wang, R., & Lu, T. (2023). Quantifying water impoundment-driven air temperature changes in the Dammed Jinsha River, Southwest China. *Remote Sensing*, *15*(17), 4280. https://doi.org/10.3390/rs15174280

Liang, S. (2001). Narrowband to broadband conversions of land surface albedo I: Algorithms. *Remote Sensing of Environment*, *76*(2), 213–238. https://doi.org/10.1016/S0034-4257(00)00205-4

Manninen, T., & Jääskeläinen, E. (2018). The effect of snow on boreal forest Albedo. In *IGARSS 2018—2018 IEEE International Geoscience and Remote Sensing Symposium* (pp. 5184–5187). https://doi.org/10.1109/IGARSS.2018.8517671

Martynov, A., Sushama, L., Laprise, R., Winger, K., & Dugas, B. (2012). Interactive lakes in the Canadian Regional Climate Model, version 5: The role of lakes in the regional climate of North America. *Tellus A: Dynamic Meteorology and Oceanography*, *64*(1), 16226. https://doi.org/10.3402/tellusa.v64i0.16226

Meng, X., Cheng, J., Zhao, S., Liu, S., & Yao, Y. (2019). Estimating land surface temperature from Landsat-8 data using the NOAA JPSS enterprise algorithm. *Remote Sensing*, *11*(2), 155. https://doi.org/10.3390/rs11020155

Moene, A. F., & van Dam, J. C. (2014). *Transport in the atmosphere-vegetation-soil continuum*. Cambridge University Press. Retrieved from https://research.wur.nl/en/publications/transport-in-the-atmosphere-vegetation-soil-continuum

Montanaro, M., Gerace, A., Lunsford, A., & Reuter, D. (2014). Stray light artifacts in imagery from the Landsat 8 thermal infrared sensor. *Remote Sensing*, *6*(11), 10435–10456. https://doi.org/10.3390/rs61110435

Murphy, S. (2018). *samsammurphy/gee-atmcorr-S2*. Jupyter Notebook. Retrieved from https://github.com/samsammurphy/gee-atmcorr-S2

Naegeli, K., Damm, A., Huss, M., Wulf, H., Schaepman, M., & Hoelzle, M. (2017). Cross-comparison of albedo products for glacier surfaces derived from airborne and satellite (Sentinel-2 and Landsat 8) optical data. *Remote Sensing*, *9*(2), 110. https://doi.org/10.3390/rs9020110

Natural Resources Canada. (2024). Hydroelectric energy. Retrieved from https://natural-resources.canada.ca/energy-sources/renewable-energy/hydroelectric-energy

Nguyen, M. D., Baez-Villanueva, O. M., Bui, D. D., Nguyen, P. T., & Ribbe, L. (2020). Harmonization of Landsat and Sentinel 2 for crop monitoring in drought prone areas: Case studies of Ninh Thuan (Vietnam) and Bekaa (Lebanon). *Remote Sensing*, *12*(2), 281. https://doi.org/10.3390/rs12020281

Nordbo, A., Launiainen, S., Mammarella, I., Leppäranta, M., Huotari, J., Ojala, A., & Vesala, T. (2011). Long-term energy flux measurements and energy balance over a small boreal lake using eddy covariance technique. *Journal of Geophysical Research*, *116*(D2), D02119. https://doi.org/10.1029/2010JD014542

Onwukwe, C., Jackson, P., Islam, S., Déry, S., Menounos, B., Marini, K., & Tilson, M. (2024). Climatic effects of the Williston Reservoir on Tsay Keh Dene Nation Territory of northern British Columbia, Canada. *Climatic Change*, *177*(2), 23. https://doi.org/10.1007/s10584-024-03683-9

Patel, S., & Rix, A. (2019). Water surface albedo modelling for floating PV plants. In *6th Southern African Solar Energy Conference (SASEC), Port Alfred, South Africa* (Vol. 19).

Pierre, A., Nadeau, D. F., Thiboult, A., Rousseau, A. N., Tremblay, A., Isabelle, P.-E., & Anctil, F. (2023). Characteristic time scales of evaporation from a subarctic reservoir. *Hydrological Processes*, *37*(3), e14842. https://doi.org/10.1002/hyp.14842

Ponce, V. M., Lohani, A. K., & Huston, P. T. (1997). Surface albedo and water resources: Hydroclimatological impact of human activities. *Journal of Hydrologic Engineering*, *2*(4), 197–203. https://doi.org/10.1061/(ASCE)1084-0699(1997)2:4(197)

Poortinga, A., Tenneson, K., Shapiro, A., Nquyen, Q., San Aung, K., Chishtie, F., & Saah, D. (2019). Mapping plantations in Myanmar by Fusing Landsat-8, Sentinel-2 and Sentinel-1 data along with systematic error quantification. *Remote Sensing*, *11*(7), 831. https://doi.org/10.3390/rs11070831

Qu, Y., Liang, S., Liu, Q., He, T., Liu, S., & Li, X. (2015). Mapping surface broadband albedo from satellite observations: A review of literatures on algorithms and products. *Remote Sensing*, *7*(1), 990–1020. https://doi.org/10.3390/rs70100990

Roy, D. P., Zhang, H. K., Ju, J., Gomez-Dans, J. L., Lewis, P. E., Schaaf, C. B., et al. (2016). A general method to normalize Landsat reflectance data to nadir BRDF adjusted reflectance. *Remote Sensing of Environment*, *176*, 255–271. https://doi.org/10.1016/j.rse.2016.01.023

Salih, M., Jasim, O., Hassoon, K., & Abdalkadhum, A. (2018). Land surface temperature retrieval from LANDSAT-8 thermal infrared sensor data and validation with infrared thermometer camera.

Samuelsson, P., Kourzeneva, E., & Mironov, D. (2010). The impact of lakes on the European climate as simulated by a regional climate model. *Boreal Environment Research*, *15*, 113–129.

Soenen, S. A., Peddle, D. R., & Coburn, C. A. (2005). SCS+C: A modified Sun-canopy-sensor topographic correction in forested terrain. *IEEE Transactions on Geoscience and Remote Sensing*, *43*(9), 2148–2159. https://doi.org/10.1109/TGRS.2005.852480

Stathopoulou, M., & Cartalis, C. (2007). Daytime urban heat islands from Landsat ETM+ and Corine land cover data: An application to major cities in Greece. *Solar Energy*, *81*(3), 358–368. https://doi.org/10.1016/j.solener.2006.06.014

Storey, J., Scaramuzza, P., Schmidt, G., & Barsi, J. (2005). Landsat 7 scan line corrector-off gap-filled product development.

Subin, Z. M., Riley, W. J., & Mironov, D. (2012). An improved lake model for climate simulations: Model structure, evaluation, and sensitivity analyses in CESM1. *Journal of Advances in Modeling Earth Systems*, *4*(1). https://doi.org/10.1029/2011MS000072

Traversa, G., Fugazza, D., Senese, A., & Frezzotti, M. (2021). Landsat 8 OLI broadband albedo validation in Antarctica and Greenland. *Remote Sensing*, *13*(4), 799. https://doi.org/10.3390/rs13040799

Vermote, E. F., Tanre, D., Deuze, J. L., Herman, M., & Morcette, J.-J. (1997). Second simulation of the satellite signal in the solar spectrum, 6S: An overview. *IEEE Transactions on Geoscience and Remote Sensing*, *35*(3), 675–686. https://doi.org/10.1109/36.581987

Walawender, J. P., Szymanowski, M., Hajto, M. J., & Bokwa, A. (2014). Land surface temperature patterns in the urban agglomeration of Krakow (Poland) derived from Landsat-7/ETM+ data. *Pure and Applied Geophysics*, *171*(6), 913–940. https://doi.org/10.1007/s00024-013-0685-7

Wang, L., Lu, Y., & Yao, Y. (2019). Comparison of three algorithms for the retrieval of land surface temperature from Landsat 8 images. *Sensors*, *19*(22), 5049. https://doi.org/10.3390/s19225049

Warren, S. G. (1982). Optical properties of snow. *Reviews of Geophysics*, *20*(1), 67–89. https://doi.org/10.1029/RG020i001p00067

Wilson, R. T. (2013). Py6S: A Python interface to the 6S radiative transfer model. *Computers & Geosciences*, *51*, 166–171. https://doi.org/10.1016/j.cageo.2012.08.002

Wiscombe, W. J., & Warren, S. G. (1980). A model for the spectral albedo of snow. I: Pure snow. *Journal of the Atmospheric Sciences*, *37*(12), 2712–2733. https://doi.org/10.1175/1520-0469(1980)037<2712:AMFTSA>2.0.CO;2

Wohlfahrt, G., Tomelleri, E., & Hammerle, A. (2021). The albedo–climate penalty of hydropower reservoirs. *Nature Energy*, *6*(4), 372–377. https://doi.org/10.1038/s41560-021-00784-y

Wulder, M. A., Roy, D. P., Radeloff, V. C., Loveland, T. R., Anderson, M. C., Johnson, D. M., et al. (2022). Fifty years of Landsat science and impacts. *Remote Sensing of Environment*, *280*, 113195. https://doi.org/10.1016/j.rse.2022.113195

Zhang, H. K., Roy, D. P., Yan, L., Li, Z., Huang, H., Vermote, E., et al. (2018). Characterization of Sentinel-2A and Landsat-8 top of atmosphere, surface, and nadir BRDF adjusted reflectance and NDVI differences. *Remote Sensing of Environment*, *215*, 482–494. https://doi.org/10.1016/j.rse.2018.04.031

Zhu, X., Liu, D., & Chen, J. (2012). A new geostatistical approach for filling gaps in Landsat ETM+ SLC-off images. *Remote Sensing of Environment*, *124*, 49–60. https://doi.org/10.1016/j.rse.2012.04.019